ACS Photonics
Article
pubs.acs.org/journal/apchd5

Enhancing Optical Nonlinearity in a Nonstoichiometric SiN Waveguide for Cross-Wavelength All-Optical Data Processing

Chung-Lun Wu, Yung-Hsiang Lin, Sheng-Pin Su, Bo-Ji Huang, Cheng-Ting Tsai, Huai-Yung Wang, Yu-Chieh Chi, Chih-I Wu, and Gong-Ru Lin*

Graduate Institute of Photonics and Optoelectronics and Department of Electrical Engineering, National Taiwan University (NTU), 1, Roosevelt Road Sec. 4, Taipei 10617, Taiwan R.O.C.

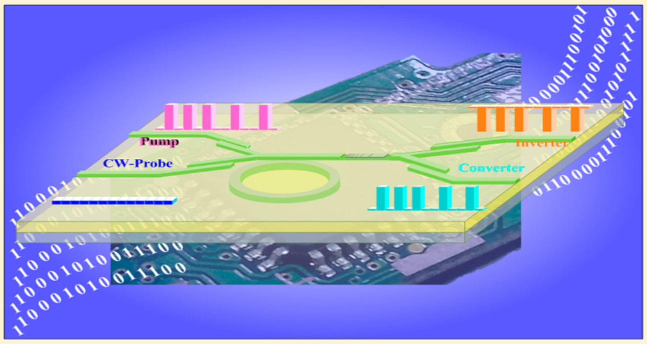

ABSTRACT: Nonstoichiometric SiN_x with enhancing optical nonlinearity is enabled to facilitate the waveguide microring resonator for cross-wavelength all-optical data processing applications. The Si/N composition ratio of the nonstoichiometric SiN_x can be detuned from stoichiometric to Si-rich by adjusting the SiH_4/NH_3 fluence ratios. Under pumping with incoming pulsed data, the comb-like transmittance of the nonstoichiometric SiN_x microring resonator can spectrally red-shift by 100 pm as its effective refractive index changed by more than 1 order of magnitude due to the enhanced nonlinear Kerr effect. The enlarged refractive index of $\Delta n = 1.6 \times 10^{-4}$ with increasing nonlinear refractive index to $n_2 = 1.6 \times 10^{-13}$ cm^2/W at 1550 nm is observed at a Si concentration of 66.2% in the Si-rich SiN_x film. In application, a cross-wavelength all-optical data conversion/inversion processor based on the nonstoichiometric SiN_x microring resonator is presented. The dense nanoscale Si content formed by a higher Si/N composition ratio of the SiN_x contributes to an enhanced Kerr effect based optical nonlinear switching, which enables the optimized 12 Gbit/s all-optical conversion of the pulsed return-to-zero on−off-keying (RZ-OOK) data with converted or inverted format. The photon lifetime of ~19 ps in the Si-rich SiN_x microring resonator cavity can support the Si-rich SiN_x all-optical Kerr switch with a maximal bandwidth of up to 50 GHz.

KEYWORDS: *data conversion, format inversion, Si-rich SiN_x, Si/N composition ratio microring resonator, all-optical modulation, nonlinear Kerr switching*

Silicon photonics has been considered to realize the optical interconnect circuits for decades, and the pure Si-based waveguide devices have played important roles in acting as different functionalities in this field. With the free-carrier-induced plasma dispersion effect,[1,2] a pure Si-based electro-optical modulator and all-optical modulators were demonstrated.[3−7] The all-optical modulation bandwidth extended from hundreds of MHz to several GHz but was limited by the carrier diffusion dominated lifetime of the bulk Si.[8,9] Recently, the free-carrier absorption (FCA) cross-section in the silicon quantum dots (Si-QDs) has been proved to be 1 order of magnitude larger than that in the bulk Si.[10−12] Even though shrinking the Si-QD size can further shorten the carrier relaxation lifetime due to the quantum confinement effect,[13,14] the effective free-carrier lifetime in Si-QDs is still much longer than that of the bulk Si so as to limit the modulation bandwidth of the Si-QD-based FCA modulator at around 1 MHz.[15−17] To develop an ultrafast all-optical modulator that is fully compatible with Si-based CMOS integrated circuits, the most appropriate solution among versatile approaches is to use the enhanced optical nonlinearity of the Si-QDs. Recently, the optical nonlinearity of the Si-QDs doped in SiO_x has been analyzed by using the femtosecond Z-scan method.[18−21] The nonlinear Kerr coefficient of the Si-QDs is experimentally proved to be 2 orders of magnitude higher than that of the bulk Si due to the strong quantum confinement effect.[18−22] The excitons generated in the highly confined Si-QDs result in the enhanced oscillating strength to increase its third-order susceptibility.[18,23] Such an enhanced nonlinear property has been utilized to demonstrate four-wave-mixing (FWM) and nonlinear Kerr switching by using the SiO_x:Si-QD-based slot waveguide.[24−26] However, the refractive index of SiO_x:Si-QD is typically between 1.6 and 1.8, which makes the refractive index difference between the SiO_x core and SiO_2 cladding very small, thus inducing the difficulty to design a channel waveguide structure with high optical confinement. This explains the reason that most of the SiO_x:Si-QD devices used for demonstrating the FWM or Kerr switching functionality are made with a slot waveguide structure. Although the slot waveguide structure achieves high optical confinement of the optical field in the ultrasmall SiO_x:Si-QD core, the large coupling losses between the slot waveguide and lensed fiber causes another drawback; however, there are well-established

Received: April 13, 2015
Published: July 24, 2015

DOI: 10.1021/acsphotonics.5b00192
ACS Photonics 2015, 2, 1141−1154

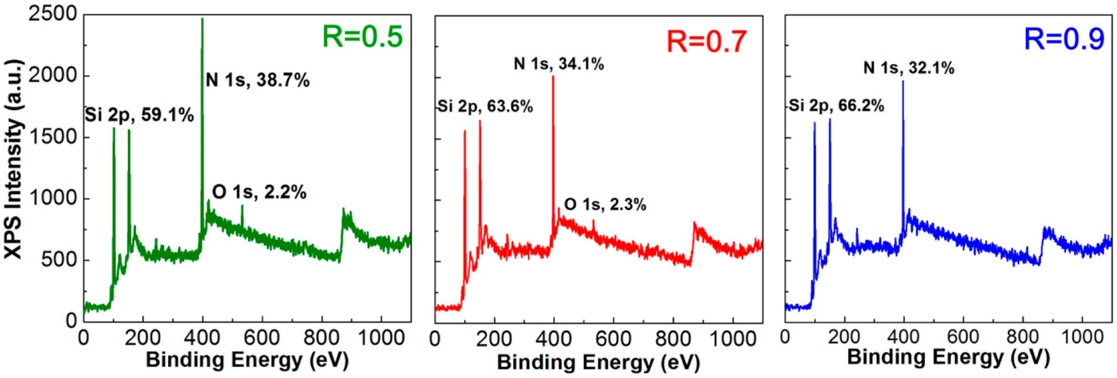

Figure 1. XPS spectra of the Si-rich SiN_x films grown with different SiH_4/NH_3 fluence ratios.

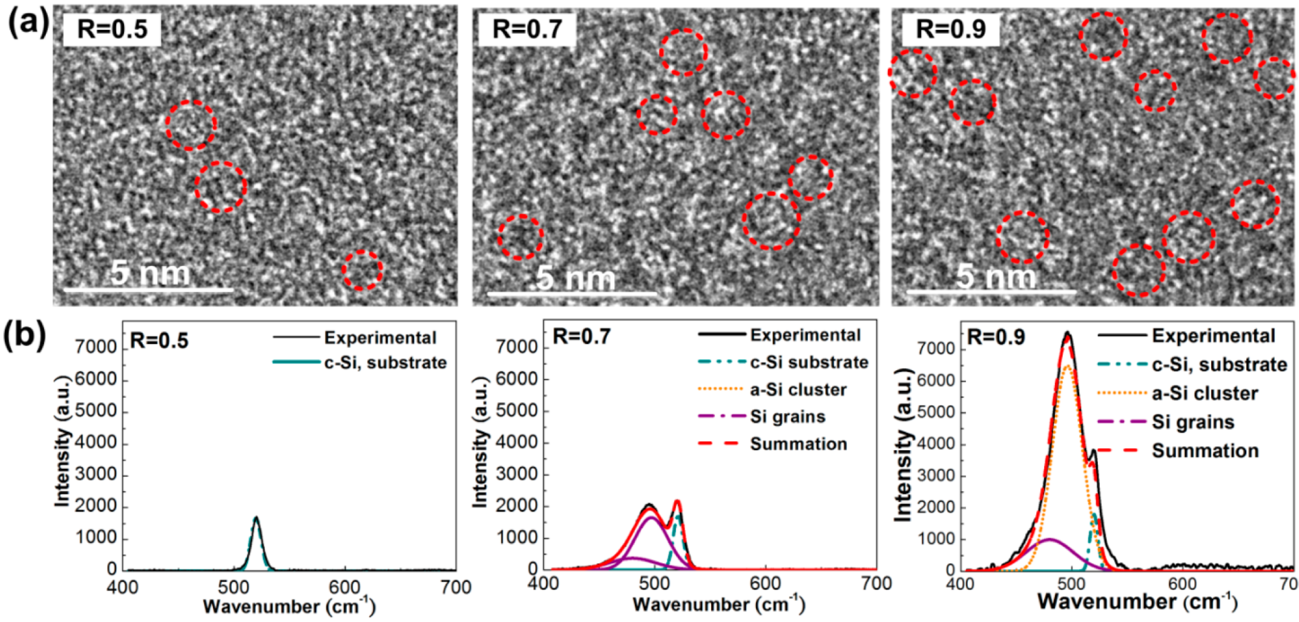

Figure 2. (a) TEM images and (b) Raman scattering spectra of the Si-rich SiN_x films grown with different SiH_4/NH_3 fluence ratios.

methods to overcome this problem. Alternatively, a host matrix with high refractive index should be carefully selected to fabricate a highly confined Si-QD incorporated dielectric channel waveguide. In view of the potential candidates, silicon nitride (Si_3N_4) is one of the alternatives that exhibit sufficiently high refractive index and large optical nonlinearity, which is free of two-photon absorption and can lead to ultralow propagation loss after forming the $SiO_2/Si_3N_4/SiO_2$ channel waveguide geometry. By using the stoichiometric Si_3N_4 channel waveguide,[27−29] the FWM, self-phase modulation, and nonlinear Kerr switching were successively realized but with insufficient throughput. Apparently, enhancement of the nonlinear refractive index of Si_3N_4 ($\sim 10^{-15}$ cm^2/W) is necessary to improve the performances of the aforementioned nonlinear devices. If the amorphous Si-QD can be doped into the Si-rich SiN_x matrix, it is believed that the optical nonlinearity of the Si-rich SiN_x film can be enhanced significantly according to the prediction by the quantum confinement effect.

In this work, the effect of the Si/N composition ratio on the nonlinear Kerr switching efficiency of a Si-rich SiN_x microring waveguide resonator is investigated. The Si-rich SiN_x film with enhanced optical nonlinearity by raising its Si/N ratio is employed to optimize the all-optical data conversion and format inversion. With the intense incoming pump data, the transiently shifted transmittance spectrum induced by the nonlinear Kerr effect in the Si-rich SiN_x film based microring resonator leads to a significant cross-wavelength switching of the continuous-wave probe. Even if the refractive index change is very small, the difference on transmittance in the microring resonator at a specific probe wavelength can be maximized by precisely adjusting either the pump power or the probe wavelength. In that case, all-optical data conversion and format inversion can be demonstrated after passing through the Si-rich SiN_x microring resonator. By precisely matching the probe wavelength with the original or the shifted notch of the resonant transmittance, the continuous-wave probe signal can be directly cross-wavelength modulated with its format either converted or inverted with respect to the pump data stream. As a result, the all-optical data conversion/inversion with the pulsed return-to-zero on−off-keying (RZ-OOK) data format at up to 12 Gbit/s can be achieved based on the ultrafast nonlinear Kerr switching induced all-optical data encoding in the Si-rich SiN_x microring resonator.

RESULTS AND DISCUSSION

X-ray Photoelectron Spectroscopy, Transmission Electron Microscopy, and Raman Spectra of the Si-Rich SiN_x. The Si-rich SiN_x films were deposited by using plasma-enhanced chemical vapor deposition (PECVD) with reaction gases mixed with SiH_4 and NH_3. During the synthesis, the RF plasma power is set as 100 W and the substrate temperature remains constant at 350 °C. By changing the fluence ratio R (defined as $R = [SiH_4]/[NH_3]$) from 0.5 to 0.9 under the same chamber pressure of 134 Pa, the Si/N atomic composition ratio in the Si-rich SiN_x films can be controlled. The thickness of the Si-rich SiN_x films for different fluence ratios was kept the same at ~600 nm for comparison. The atomic compositions of the Si-rich SiN_x films with different SiH_4/NH_3 fluence ratios characterized by X-ray photoelectron spectroscopy are shown in Figure 1a. The Si concentration is increased from 59.1% to 66.2% when increasing the SiH_4/NH_3 fluence ratio from $R = 0.5$ to $R = 0.9$.

The transmission electron microscopy (TEM) images of the Si-rich SiN_x films grown with different SiH_4/NH_3 fluence ratios are demonstrated in Figure 2a. The TEM images confirm the formations of amorphous Si-QDs in Si-rich SiN_x films. When the Si concentration is increased from 59.1% to 66.2% by increasing the SiH_4/NH_3 fluence ratio from $R = 0.5$ to $R = 0.9$, only the volume density of Si-QD increases from 8×10^{18} to 5×10^{19} #/cm^3, and the average size of the Si-QD remains at 0.9 nm. To confirm the existence of Si-QDs, the Raman scattering spectra of the Si-rich SiN_x with $R = 0.5$, $R = 0.7$, and $R = 0.9$ are shown in Figure 2b, which are decomposed by multi-Gaussian functions to distinguish the contributions from different bonding components and structures. The common peak at a wavenumber of 520 cm^{-1} with a full-width at half maximum (fwhm) of 10 cm^{-1} is originated from the Si substrate.[30] For the Si-rich SiN_x films grown with $R = 0.7$ and 0.9, there are two broadened spectral peaks. The first peak, located at 495 cm^{-1} with an fwhm of 21 cm^{-1}, is attributed to the amorphous Si clusters self-assembled in the Si-rich SiN_x film.[31] The second peak, at 480 cm^{-1} with an fwhm of 31 cm^{-1}, comes from the Si grains in the Si-rich SiN_x films.[32] Due to the dilute Si-QDs, the related spectral components are too weak to be observed from the Si-rich SiN_x film with $R = 0.5$. When increasing the SiH_4/NH_3 fluence ratio from $R = 0.5$ to $R = 0.9$, the enhanced Raman scattering intensities of the amorphous Si nanoclusters and Si micrograins indicate that their densities are concurrently enriched in the Si-rich SiN_x films with increasing Si/N composition ratio.

For device fabrication, the Si-rich SiN_x films with different Si/N composition ratios are utilized to serve as the core layer of the channel waveguide in the bus coupler and the microring resonator. First of all, a Si-rich SiN_x film with a thickness of 400 nm is deposited on a 3 μm thick thermal oxide covered Si wafer. Then, e-beam lithography is utilized to define the bus line and microring resonator patterns on the Si-rich SiN_x film coated with photoresist (ZEP, 520A). The width of the waveguide is 600 nm, and the radius of the microring resonator is 150 μm. The gaps between the bus and microring waveguides for Si-rich SiN_x films with $R = 0.5$, $R = 0.7$, and $R = 0.9$ are set as 900, 800, and 300 nm, respectively, due to the differences of their refractive indices. In particular, the inverse tapered structures are employed at the both end facets of the bus line waveguides to enhance the power coupling efficiency between the waveguides and lensed fibers. The width of the inverse taper is increased from 200 nm to 600 nm within a length of 200 μm. Afterward, the Cr layer with a thickness of 80 nm is evaporated on the photoresist patterned wafer to serve as a hard mask by using e-gun evaporation. Subsequently, a patterned Si-rich SiN_x waveguide is formed by using a reactive ion etching (RIE) system under a flowing $CHF_3 + O_2$ gaseous mixture. After cleaning the Cr by chemical etchant, a 2 μm thick SiO_2 film is deposited on the Si-rich SiN_x bus and microring waveguides to serve as the cladding layer. Finally, both ends of the waveguide are cleaved and polished, and the top-view scanning electron microscope (SEM) image of the Si-rich SiN_x bus and microring waveguide geometry is shown in Figure 3.

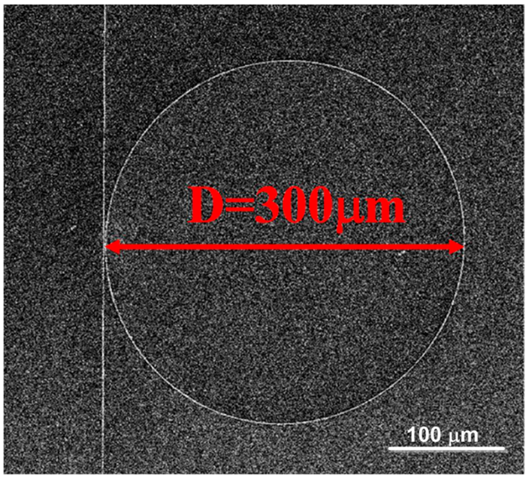

Figure 3. Top-view SEM image of the Si-rich SiN_x microring resonator.

Mode Property and Kerr Switching Effect in the Si-Rich SiN_x Microring Resonator. The refractive index spectra of the Si-rich SiN_x films grown with different SiH_4/NH_3 fluence ratios are measured by using an ellipsometer as shown in Figure 4a. In Figure 4b, by setting the identical width and height of the Si-rich SiN_x based channel waveguide as 600 and 400 nm, respectively, and detuning the gap between the ring and bus waveguide as 900 nm for Si-rich SiN_x with $R = 0.5$, 800 nm for Si-rich SiN_x with $R = 0.7$, and 300 nm for Si-rich SiN_x with $R = 0.9$, the simulated fundamental TE modes at 1550 nm are shown in Figure 4c.

The measured and simulated transmission spectra of the microring resonators made by three different Si-rich SiN_x samples are shown in Figure 5. Note that the group indices of the Si-rich SiN_x are increased from 2.01 to 2.49 by increasing the fluence ratio R from 0.5 to 0.9. The propagation losses in the microring cavity for the three cases are almost identical (~1.3 dB/mm), indicating that the bending loss for the microring resonator with a diameter of 300 μm is similar in each case. The propagation loss of the Si-rich SiN_x waveguide was measured by using the cut-back method. Three Si-rich SiN_x waveguides with lengths of 3, 5, and 9 mm were involved in the measurements of the cut-back method. The propagation loss in the Si-rich SiN_x channel waveguide determined as ~1 dB/cm is smaller than that in the microring resonator. In the experiment, the scattering loss is the major contribution to the propagation loss of the Si-rich SiN_x waveguide, which is induced by the imperfect sidewall of the waveguide caused during lift-off or the RIE process. According to the absorption spectroscopy, the

DOI: 10.1021/acsphotonics.5b00192
ACS Photonics 2015, 2, 1141−1154

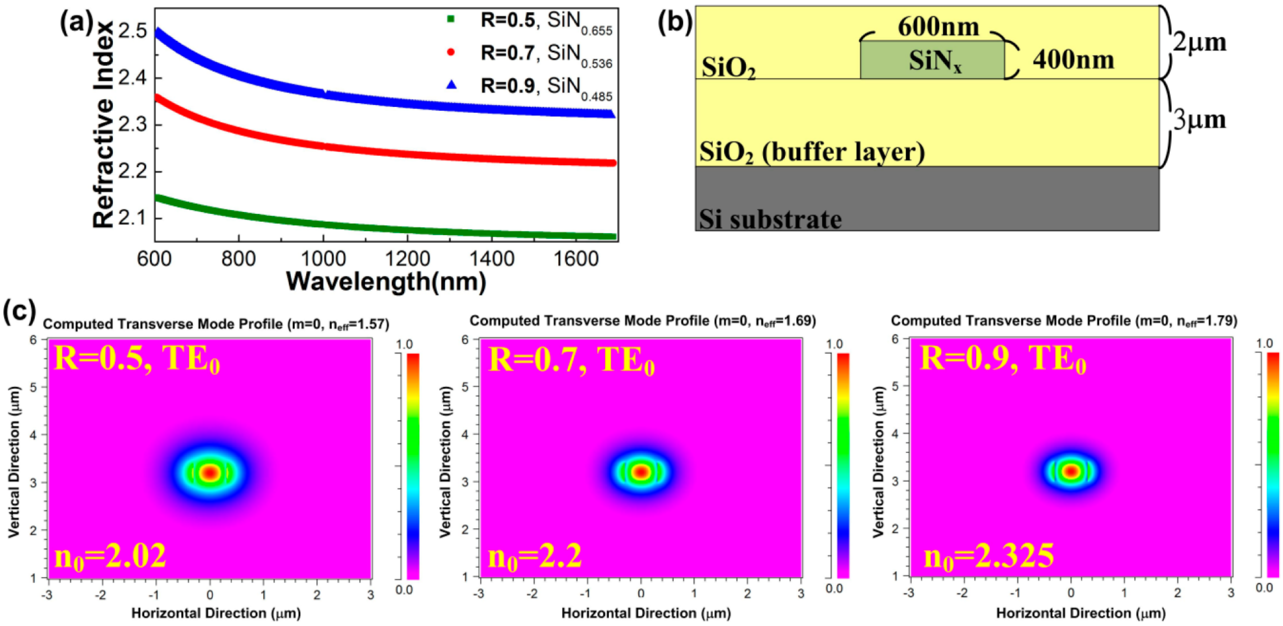

Figure 4. (a) Refractive index spectra of the Si-rich SiN_x films. (b) Geometry of the Si-rich SiN_x channel waveguide. (c) Simulated fundamental TE modes at 1550 nm for different SiN_x samples.

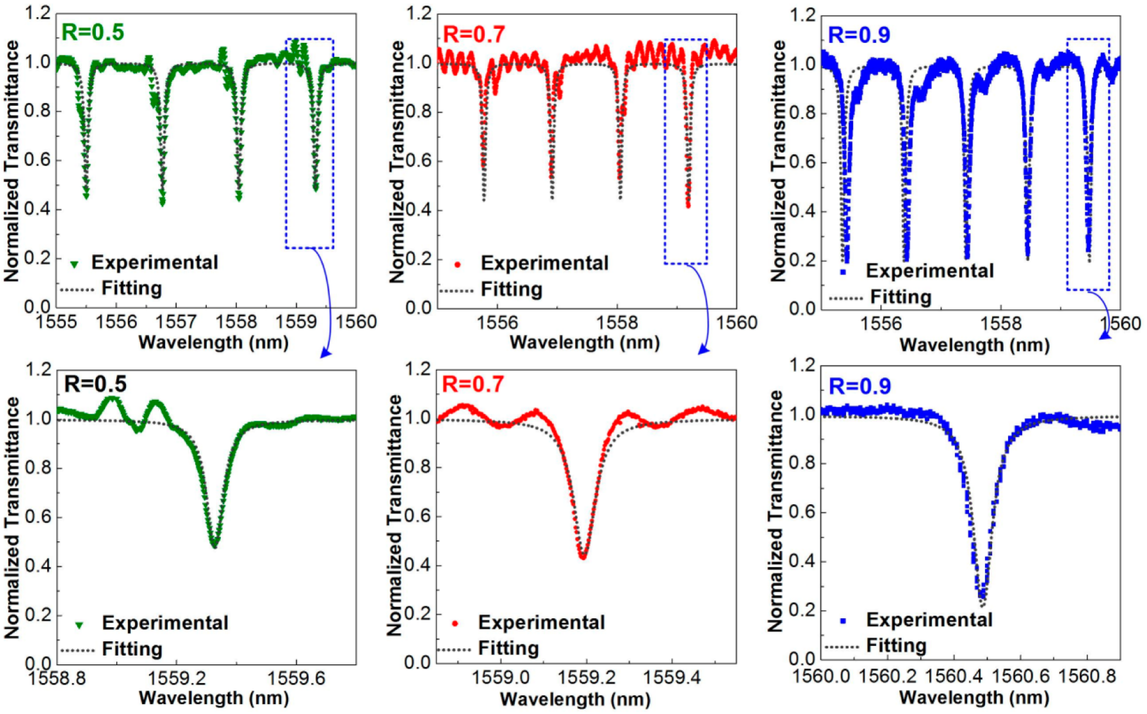

Figure 5. Transmission spectra of the Si-rich SiN_x microring resonators and the corresponding fitting curve.

absorption loss of the Si-rich SiN_x film is extremely small at a wavelength of 1550 nm (see Figure 6), thus providing less contribution to the propagation loss of the Si-rich SiN_x waveguide when comparing with the scattering effect. The quality factors for the three cases are all around ~25 000. By using eq 5 (refer to the Methods section) to estimate the optical intensity enhancement of the pump beam in the microring resonator, the intensity magnification factor of the Si-rich SiN_x microring resonator can be determined by employing the fitting parameters for the Si-rich SiN_x microring resonator shown in Table 1.

The operating principle of a microring resonator based nonlinear Kerr switch is illustrated in Figure 7. The pump beam is an optical pulse with high peak power, and the pump wavelength is set to coincide with the transmission dip caused by the microring resonator. Therefore, the peak power of the pump pulse will be coupled into and built up in the microring resonator, and the refractive index in the microring waveguide will be effectively modified by the pump pulse induced Kerr nonlinearity. When the pulse is temporally turned on, the positive nonlinear refractive index change in the microring waveguide will be transiently induced to red-shift the notched

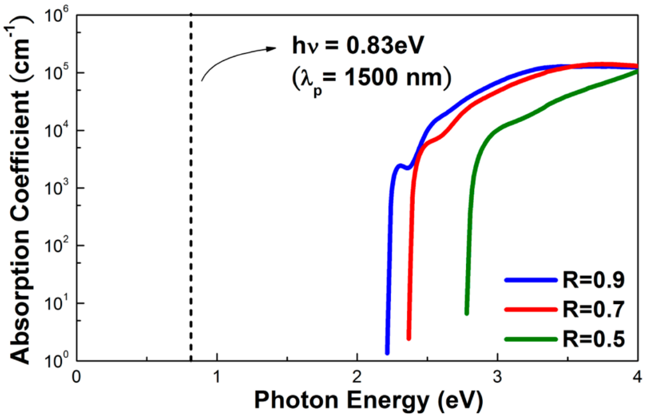

Figure 6. Linear absorption spectra of Si-rich SiN_x with different SiH_4/NH_3 fluence ratios.

Table 1. Optical Properties and Simulated Parameters of the Si-Rich SiN_x Ring Resonator

	R = 0.5	R = 0.7	R = 0.9
gap (μm)	0.9	0.8	0.3
radius of ring waveguide (μm)	150	150	150
N, group index	2.01	2.26	2.49
K, coupling ratio	0.2221	0.233 33	0.324 04
α_{ring} (dB/mm)	1.38	1.2	1.3
$\delta\lambda$, fwhm (nm)	0.073	0.06	0.064
$\Delta\lambda$, FSR (nm)	1.21	1.14	1.03
quality factor, Q	24 388	26 790	24 019
intensity magnification, M	1.78	1.91	2.47

dip in the transmission spectrum of the microring resonator. On the other hand, the refractive index in the microring resonator will resume back to the initial condition when the pulse is temporally turned off. With digitally modifying the refractive index of the microring resonator by the intense pump data stream, the all-optical data conversion and format inversion of the incoming data stream can be demonstrated at the coupled output of the microring resonator. For the data conversion shown in Figure 7a, the wavelength of the continuous-wave probe beam is set at another transmission dip of the microring resonator. In this case, the transmittance of the probe is extremely low when turning off the pump data, whereas the probe transmittance is maximized when turning on the pump to red-shift the notched dip away from the probe wavelength. For the data inversion shown in Figure 7b, the wavelength of the probe beam is slightly deviated from the transmission dip. This results in the largest transmittance at probe wavelength when turning off the pump data. If the pump data are switched on, the increased refractive index of the microring resonator causes the transmission dip to red-shift to the probe wavelength, and the probe transmittance is suddenly minimized so as to consequently obtain the inversed data stream.

Estimation of Nonlinear Refractive Index and Demonstration of All-Optical Modulation in the Transiently Pumped Si-Rich SiN_x Microring Resonator. Figure 8a shows the variation on the single-pulse-modulated probe traces obtained at the output port of the Si-rich SiN_x based microring resonator (R = 0.9) by tuning the probe wavelength from 1560.48 nm to 1560.60 nm. The pump wavelength of 1555.44 nm is located at the adjacent transmission dip of the microring resonator. By slightly detuning the probe wavelength from 1560.48 nm to 1560.52 nm, the intensity of the modulated probe is gradually decreased to zero. When further scanning the probe wavelength to 1560.54 nm, the modulated probe signal trace becomes inverted. The maximal inverted probe trace appears when shifting the probe wavelength to 1560.58 nm. As a result, the modulated probe power versus the probe wavelength is plotted in Figure 8b. The power deviation between the probe wavelength responsible for the maximized positive and negative peak power is ~0.1 nm, indicating that the transmission dip of the Si-rich SiN_x microring resonator is transiently red-shifted to 0.1 nm when the pump pulse is built up and magnified in the microring resonator. The transmission spectra with and without the pump are shown in Figure 8c. The 0.1 nm red-shift on the transmission spectrum can be correlated with the nonlinear refractive index change of 1.6×10^{-4}. With the total insertion loss contributed by the 3 dB coupler and lensed fiber of 6 dB, the peak pump power injected into the waveguide is about 0.75 W and the effective mode area of the waveguide is ~0.19 μm^2. For the microring resonator made by Si-rich SiN_x grown with a SiH_4/NH_3 fluence ratio of R = 0.9, the intensity magnification factor is up to 2.47 and the nonlinear refractive index is determined as 1.6×10^{-13} cm^2/W by using the equation $n_2 \approx \Delta n/(M \times I)$.

The nonlinear refractive index of 1.6×10^{-13} cm^2/W for Si-rich SiN_x (R = 0.9) at 1550 nm has been confirmed to be higher than that for bulk Si in nonresonance wavelength condition,[33] indicating that the excessive Si and the Si-QDs embedded in the SiN_x matrix can dominate the enhancement of optical nonlinearity. The incorporation of excess Si creates several kinds of defects in the host matrix, which is easily deformed under illumination of intense optical pulses, which induce structural changes and hyperpolarizability of the host matrix.[34] The nonlinear optical effect may also originate from the light-induced structural changes on interatomic distance, molecular orientation, and phase transition of excessive Si-related defects.[35]

In addition, the enhanced optical nonlinearity is also attributed to the purely bound-electronic effect of the hyperpolarizable delocalized electrons in the Si-QDs,[4,35,36] which arises from the polarization of the electronic cloud around the on-site atom with a response time of femtoseconds so as to promote the high-speed modulation.[36] The aforementioned effects are different from those caused by the optical nonlinearity in bulk Si. When increasing the excess Si content, such that the nanoscale Si transfers to the microcrystalline poly-Si structure, these effect could be suppressed or diminished to inversely reduce the optical nonlinearity. Besides, if the excess Si concentration further increases in the SiN_x, not only is the nonlinear refractive index enhanced, but also the linear and two-photon absorptions are increased to cause the absorption edge to red-shift to a longer wavelength. If the two-photon absorption (TPA)-induced free-carrier modulation appears in the microring resonator, the modulation speed will be degraded by the long relaxation lifetime of the free carriers. As evidence, Martinez and co-workers have already demonstrated that the combined Kerr and FCA effects reveal a fast Kerr response (~ps) and slow FCA-related tail (~ns) to degrade the modulation speed with distorted modulation traces.[26]

At the current conditions, the peak intensity of the pump beam coupled into the waveguide is ~0.4 GW/cm^2. Our observations indicate that the Si-rich SiN_x-based ring resonator

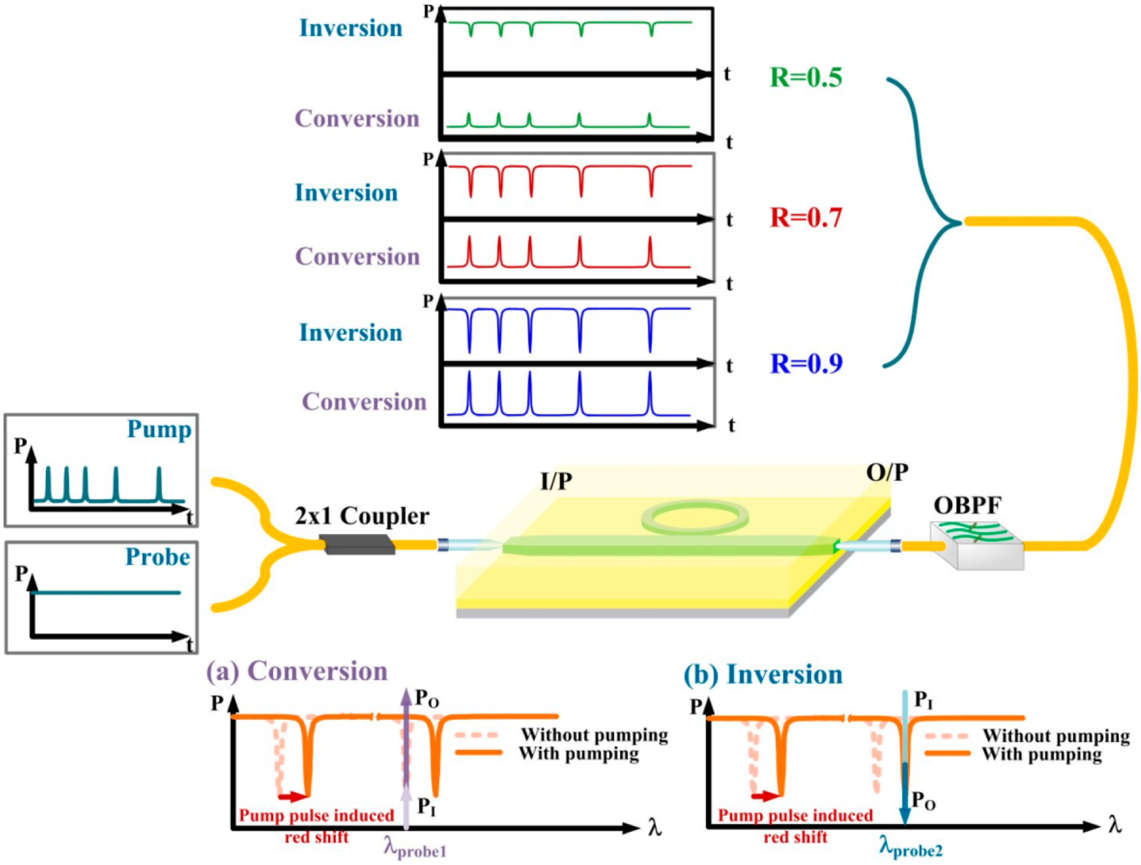

Figure 7. Schematic diagram of the SiN_x microring resonator based nonlinear Kerr switch. (a) Data-converted modulation. (b) Data-inverted modulation. (P_I: input power level, P_O: output power level. For data-converted modulation at λ_{probe1}, the transmitted power is increased with the pumping pulse due to the nonlinear Kerr effect. For data-inverted modulation at λ_{probe2}, the transmitted power is decreased with the pumping pulse due to the nonlinear Kerr effect.)

exhibits a pure Kerr response without distorting by TPA-induced FCA modulation. This ensures that Si-rich SiN_x is a potential candidate to fabricate an ultrafast all-optical data encoding and format switcher.

To confirm that there is no TPA effect existing in the Si-rich SiN_x waveguide, the waveguide is measured by analyzing its P_{out} versus P_{in} curve under intense pumping conditions. Figure 9a demonstrates the experimental setup for measuring the TPA effect in the Si-rich SiN_x channel waveguide. In the measurement, the pump pulse is generated by externally modulating a continuous-wave tunable laser at 1550 nm with a Mach—Zehnder modulator. Subsequently, the generated optical pulse is power amplified by using a first-stage erbium-doped fiber amplifier, and an optical bandpass filter (OBPF) is utilized to suppress the induced amplified spontaneous emission (ASE) noise. Another high-gain erbium-doped fiber amplifier (EDFA) serves as the second-stage boost optical amplifier to further increase the peak power of the pump pulse, and another OBPF is also utilized to suppress the ASE noise induced by the second-stage EDFA. Finally, the dual-stage amplified pump pulse with a pulse width of 83 ps and a peak power of up to 3 W is delivered for the test. The establishment of the pump pulse is described in detail as given in the Methods. The optical pump pulse is incident to the Si-rich SiN_x waveguide. By increasing the pulsed peak power up to 3 W, the plot of output versus input power still reveals a linear trend (see Figure 9b), indicating that the TPA in the Si-rich SiN_x channel waveguide is entirely eliminated under such high input power.

Based on a similar analysis, the variation on the single-pulse-modulated probe signal traces output from the Si-rich SiN_x microring resonator with $R = 0.7$ by scanning the probe wavelength is shown in Figure 10a. At the beginning, the wavelengths of the pump and probe are first set as 1555.77 and 1559.19 nm, respectively. The null probe point is obtained by detuning the wavelength from 1559.19 nm to 1559.21 nm, and the inverted probe trace reaches a maximal modulation when scanning the probe wavelength to 1559.23 nm. Note that the amplitude of the inverted probe signal decreases again by further red-shifting the probe wavelength, as shown in Figure 10b, and the probe wavelength change between the maximal positive and negative modulation is ~0.04 nm, which is smaller than that obtained in the Si-rich SiN_x microring resonator with $R = 0.9$, as confirmed by comparing the transmission spectra with and without pumping shown in Figure 10c. Such a 0.04 nm red-shifted transmission spectrum corresponds to a refractive index change of 6×10^{-5} induced by the nonlinear Kerr effect. The Si-rich SiN_x microring resonator grown with a SiH_4/NH_3 fluence ratio of $R = 0.7$ indicates that the intensity magnification factor is only 1.91, and the nonlinear refractive index of the Si-rich SiN_x is estimated as only 8×10^{-14} cm^2/W.

A weakened cross-wavelength modulation is observed for the Si-rich SiN_x microring resonator with the lowest Si/N composition ratio grown at a SiH_4/NH_3 fluence ratio of $R = 0.5$. By setting the wavelength of the pump as 1555.49 nm and scanning the probe wavelength from 1559.32 to 1559.35 nm, the single-pulse-modulated probe signal traces at different

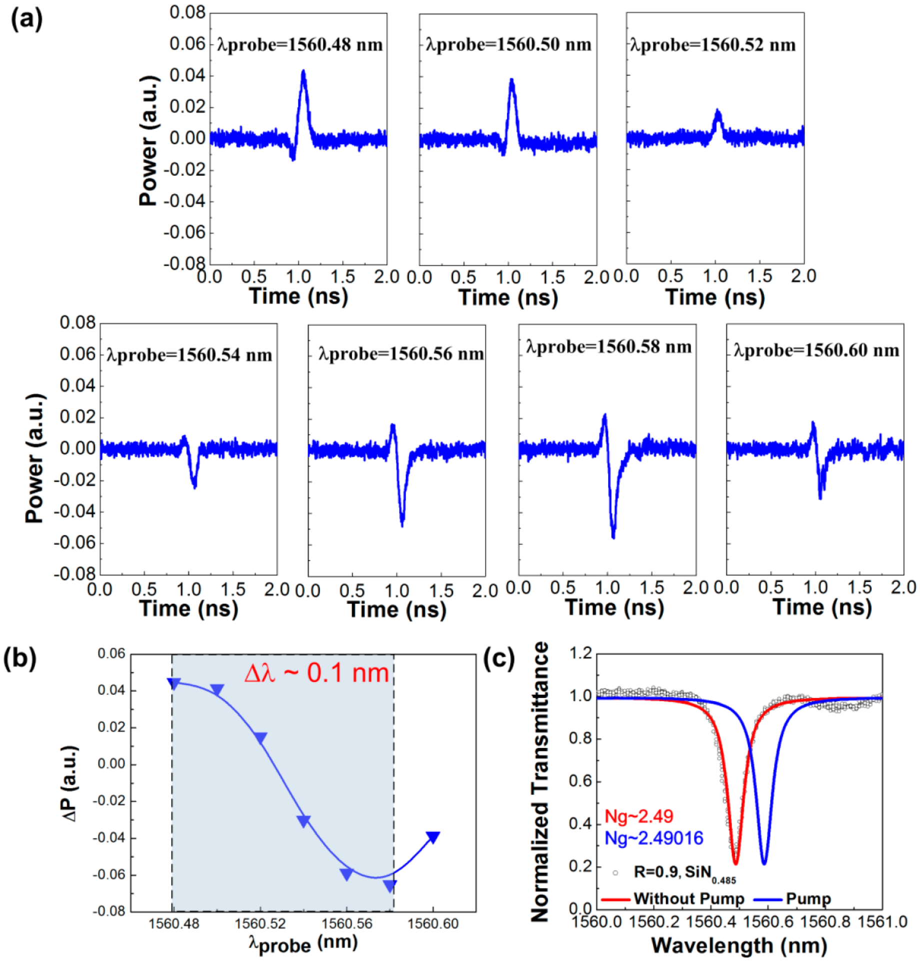

Figure 8. (a) Variation of the single-pulse-modulated probe trace output from the Si-rich SiN$_x$ microring resonator with R = 0.9. (b) Modulated probe power versus the probe wavelength. (c) Transmission spectra of the Si-rich SiN$_x$ microring resonator with and without pumping.

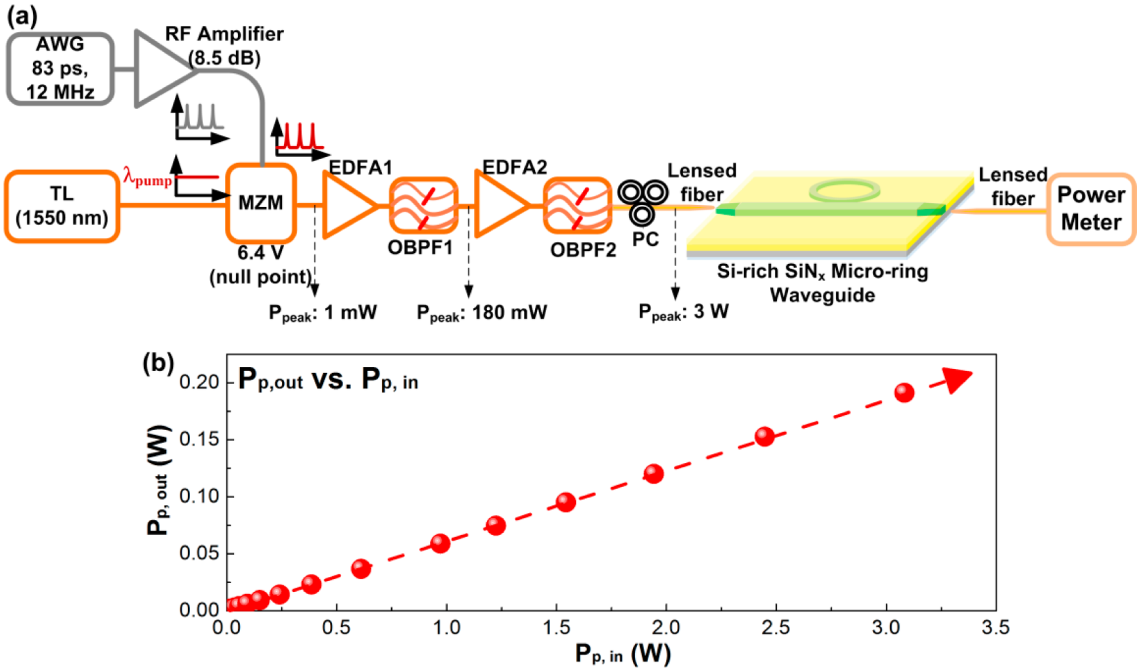

Figure 9. (a) Experimental setup for measuring the TPA effect in the Si-rich SiN$_x$ channel waveguide. (b) Output power versus input power in the Si-rich SiN$_x$ channel waveguide.

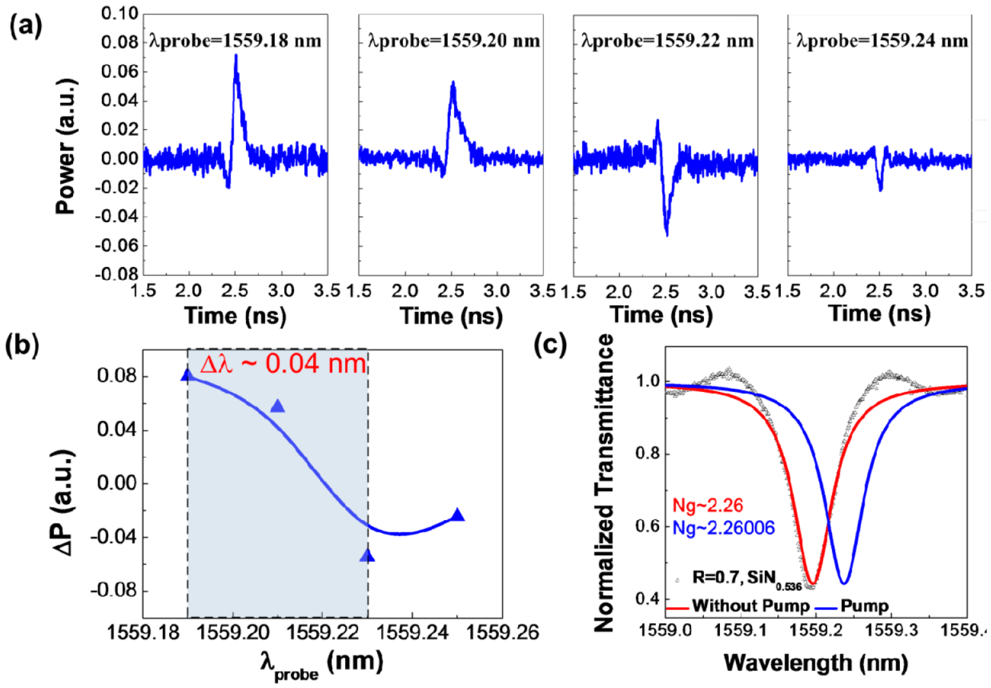

Figure 10. (a) Variation on the single-pulse-modulated probe traces output from the Si-rich SiN_x microring resonator with $R = 0.7$. (b) Modulated probe power versus the probe wavelength. (c) Transmission spectra of the Si-rich SiN_x microring resonator with and without pumping.

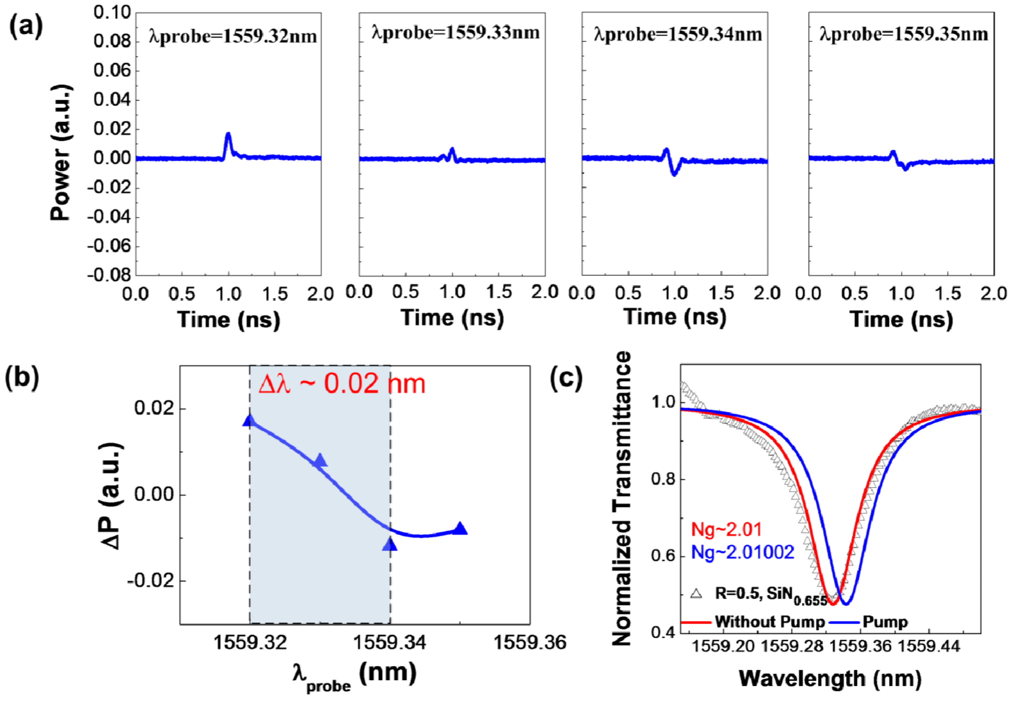

Figure 11. (a) Variation on the single-pulse-modulated probe traces output from the Si-rich SiN_x microring resonator with $R = 0.5$. (b) Modulated probe power versus the probe wavelength. (c) Transmission spectra of the Si-rich SiN_x microring resonator with and without pumping.

probe wavelengths are shown in Figure 11a. A similar sign inversion phenomenon is observed by changing the probe wavelength from 1559.32 nm to 1559.34 nm, as shown in Figure 11b. However, the modulated probe amplitude is the lowest one among all of the samples, as the nonlinear refractive index change in the Si-rich SiN_x with $R = 0.5$ is too small to compare with other samples. This causes the degraded transmittance variation and shrinks the probe wavelength to ∼0.02 nm, and the corresponding red-shift of the transmission spectra of the Si-rich SiN_x based microring resonator grown at a $\mathrm{SiH}_4/\mathrm{NH}_3$ fluence ratio of $R = 0.5$ with and without pumping are shown in Figure 11c. The intensity magnification factor in the Si-rich SiN_x microring resonator with $R = 0.5$ is as small as 1.78, providing a refractive index change of only $\sim 2 \times 10^{-5}$ under the nonlinear refractive index of 1.4×10^{-14} cm^2/W. Nevertheless, such a nonlinear refractive index of the $\mathrm{SiN}_{0.655}$ is still higher than that of the stoichiometric $\mathrm{Si}_3\mathrm{N}_4$. These observations confirm the effect of the self-assembled

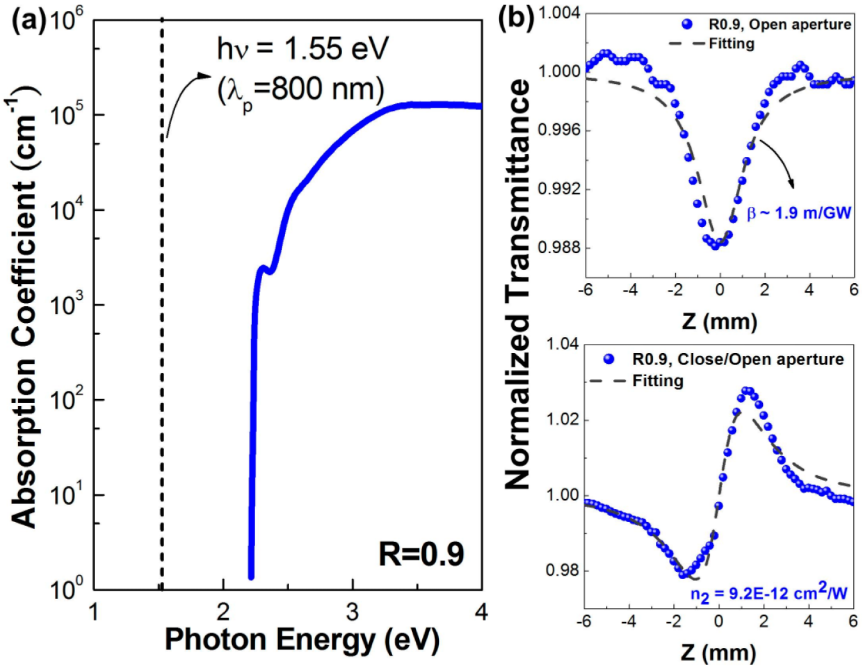

Figure 12. (a) Linear absorption spectrum of Si-rich SiN$_x$ (R = 0.9). (b) Z-scan open- and closed-aperture results of Si-rich SiN$_x$ (R = 0.9).

amorphous Si cluster on the enhanced optical nonlinearity in the Si-rich SiN$_x$ microring resonator.

In brief, the optical nonlinearity of the Si-rich SiN$_x$ films has already increased to be several orders of magnitude higher than that of the stoichiometric Si$_3$N$_4$, which can be attributed to the stronger quantum confinement effect present in the dense Si-QDs with an average size of smaller than 2 nm.[18,19] In previous works, the enhanced third-order nonlinear susceptibility ($\chi^{(3)}$) of one-dimensional Si nanowires at resonant wavelength has been theoretically estimated,[37] indicating that the $\chi^{(3)}$ can be significantly enhanced by the quantum-confined excitons occurring in the Si nanowire. The $\chi^{(3)}$ is directly proportional to the fourth-order of the center-of-mass of the quantum-confined exciton $\phi_{1s}(r)$,[37] as given by

$$\chi^{(3)} \propto |\phi_{1s}(r)|^4 \equiv \left| \left[\frac{1}{\pi a_0{}^3} \right]^{1/2} e^{-r/a_0} \right|^4 \qquad (1)$$

where a_0 is the effective Bohr radius of the quantum-confined excitons. Obviously, the correlation between the $\chi^{(3)}$ and effective Bohr radius can be simply described as $\chi^{(3)} \propto (a_0)^{-6}$. For a highly confined exciton in a nanostructure, its effective Bohr radius is significantly reduced due to the increased effective hole and electron masses in the Si nanostructure.

On the other hand, the enhanced optical nonlinearity of versatile quantum dots (such as CdS, CuBr, and InP/ZnS) in the nonresonant wavelength region has also been characterized with the photon energy confined by $E_g > h\nu > E_g/2$,[38−40] where E_g is the optical band gap of materials and $h\nu$ is the incident photon energy. Among these examples, the localized excitons in these quantum dots are excited by a two-photon absorption process, which leads to the enhanced optical nonlinearity with a high nonlinear refractive index induced by a large nonlinear absorption coefficient (TPA) in the nonresonant region.

The Z-scan analysis is also performed to demonstrate that Si-rich SiN$_x$ exhibits high optical nonlinearity. In the experiment, a Ti-sapphire laser with a central wavelength of 800 nm, a pulse width of 80 fs, and a repetition rate of 82 MHz was utilized as an excitation source. Figure 12a shows the linear absorption spectrum of Si-rich SiN$_x$ (R = 0.9) with extremely low linear absorption coefficient to confirm the nonresonance at 800 nm. The open- and closed-aperture measurements of Si-rich SiN$_x$ (R = 0.9) are shown in Figure 12b. After simulation, the nonlinear refractive index of 9.2 × 10^{-12} cm^2/W and TPA coefficient of 1.9 m/GW are determined for the Si-rich SiN$_x$ (R = 0.9) at a wavelength of 800 nm, indicating that the enhanced optical nonlinearity of Si-rich SiN$_x$ at photon energies below band gap may originate from the TPA-induced localized exciton in Si-QDs. Similar results of a high nonlinear refractive index accompanied by a large TPA coefficient in the Si-QDs embedded in a SiO$_x$ or SiN$_x$ matrix have been reported.[18,19,41]

Nevertheless, when operating the Si-rich SiN$_x$ at 1550 nm, the photon energy is far away from the absorption edge. In this case, the TPA effect at 1550 nm is much weaker than that at 800 nm. As expected, the TPA-induced FCA modulation is absent, and only the nonlinear Kerr modulation can be obtained in the Si-rich SiN$_x$-based microring resonator. The nonlinear refractive index of 1.6 × 10^{-13} cm^2/W for Si-rich SiN$_x$ (R = 0.9) at 1550 nm is higher than that of bulk-Si in the nonresonance condition.[33] It indicates that the Si nanostructure embedded in the SiN$_x$ dominates the enhancement of optical nonlinearity. Based on the aforementioned discussion, the enhanced optical nonlinearity of Si-rich SiN$_x$ at 1550 nm is not attributed to the TPA-related localized excitons in the Si-QDs, but originates from the purely bound electronic effect of the hyperpolarizable delocalized electrons in the Si-rich SiN$_x$.[20,35,36] Owing to the three-dimensional confined Si-QD nanostructure, its density-of-state function and interatomic distance are significantly changed to modify the bound electronic structure. Hence the highly distorted delocalized electron cloud induced by the hyperpolarizable delocalized electrons in the Si-QDs would enhance the optical nonlinearity of the Si-rich SiN$_x$ at below-band-gap wavelengths. The transient polarization change of the electronic cloud around the excessive Si atoms exhibits a

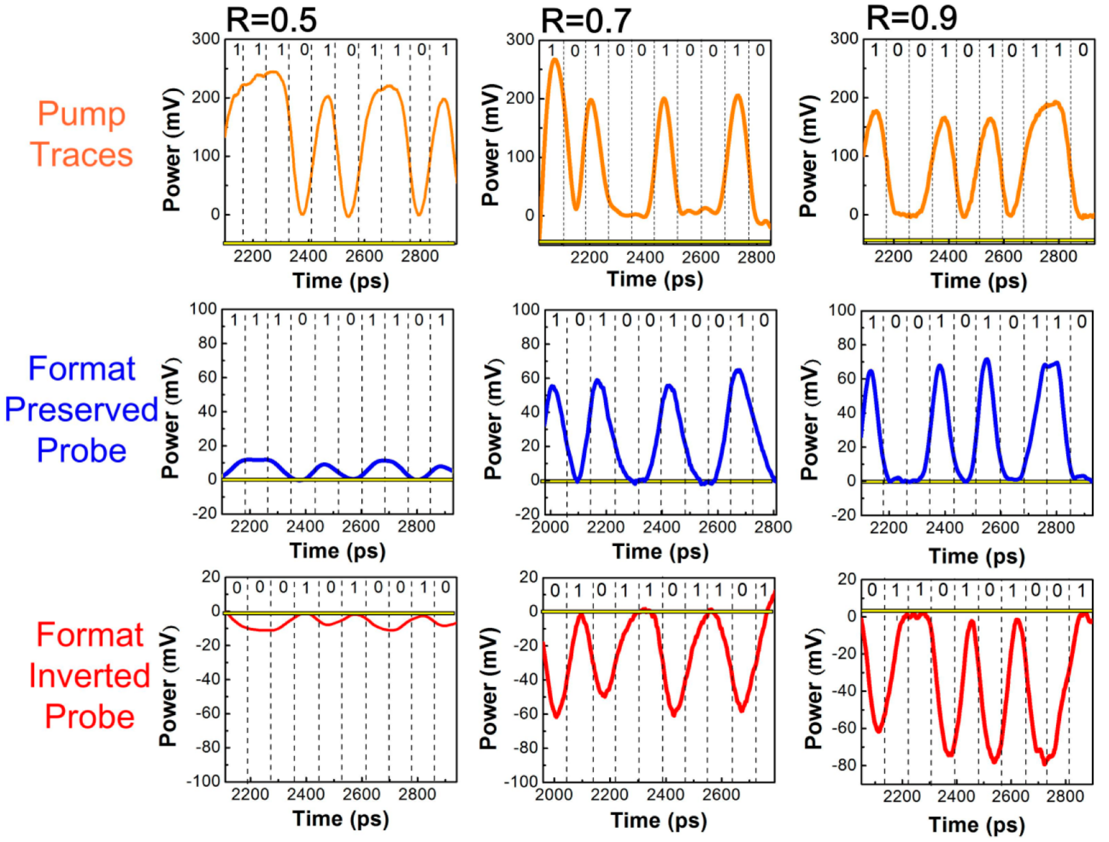

Figure 13. Upper row: Pump traces with 12 Gbit/s pulsed RZ-OOK data injected into three Si-rich SiN_x microring resonators. Middle row: Data-format preserved probe traces. Lower row: Data-format inverted probe traces.

response time of femtoseconds.[35] Therefore, the high-speed modulation beyond 10 GHz at 1550 nm is not attributed to the exciton-induced nonlinear optical effect.

As discussed, the hyperpolarizable delocalized electrons in the Si-QDs significantly enhance the optical nonlinearity at below-band-gap wavelengths. By comparing with the Si-rich SiN_x films grown with increasing the SiH_4/NH_3 fluence ratio, the nonlinear refractive index is increased by 1 order of magnitude as the Si/N composition as well as the excessive Si concentration is increased concurrently. Note that the average sizes of the amorphous Si cluster in three SiN_x samples are kept unchanged as the amorphous Si cluster is in situ formed during deposition without postannealing. In this case, the only difference among these samples is the increasing density of the amorphous Si clusters in the Si-rich SiN_x films grown with different SiH_4/NH_3 fluence ratios. As confirmed by the Raman scattering analyses, the amorphous Si cluster related Raman scattering intensity in the Si-rich SiN_x films is increased with enlarging the SiH_4/NH_3 fluence ratio during synthesis, which corroborates the increasing density of the amorphous Si clusters that is coincident with the increased excess Si concentration of the Si-rich SiN_x films grown by increasing the SiH_4/NH_3 fluence ratio. This elucidates why the nonlinear refractive index of the Si-rich SiN_x films is enhanced with increasing the SiH_4/NH_3 fluence ratio during PECVD deposition.

12 Gbit/s All-Optical Data Conversion/Inversion with Pulsed RZ-OOK Data Format in the Si-Rich SiN_x Microring Resonator. Lastly, the all-optical data conversion and format inversion of the pulsed RZ-OOK data stream is demonstrated by using the Si-rich SiN_x microring resonators. The pump traces with a pulsed RZ-OOK data format at 12 Gbit/s are shown in the first row of Figure 13. The pump wavelengths for the Si-rich SiN_x microring resonators with $R = 0.5$, $R = 0.7$, and $R = 0.9$ are set as 1555.49, 1555.77, and 1555.44 nm, corresponding to one of the resonance dips in each case. By injecting the continuous-wave probe signal into the Si-rich SiN_x microring resonator exactly at an adjacent resonance dip in each case, the pulsed RZ-OOK data stream can be wavelength converted from pump to probe carrier with its format preserved as well (refer to the second row of Figure 13). In that case, the probe wavelengths for the Si-rich SiN_x with $R = 0.5$, $R = 0.7$, and $R = 0.9$ are set as 1559.32, 1559.19, and 1560.48 nm, respectively. Furthermore, the probe carrier can also be cross-wavelength modulated by the pump data stream with its data format inverted by slightly shifting the probe wavelengths away from the on-resonant notched dip of the microring resonator, and the corresponding wavelength increment for the microring resonators made by Si-rich SiN_x with $R = 0.5$, $R = 0.7$, and $R = 0.9$ are 0.02, 0.04, and 0.1 nm, respectively. By precisely setting the probe wavelength at the transiently red-shifted resonance dip of the transmission spectra, the largest inverted modulation depth can be obtained. That is, the transmittance of the probe is completely suppressed when the pump with incoming data is injected into the Si-rich SiN_x microring resonator. For the inverse data-format conversion, the probe wavelengths are set as 1559.34, 1559.23, and 1560.58 nm for the Si-rich SiN_x with $R = 0.5$, $R = 0.7$, and $R = 0.9$, respectively (refer to the third row of Figure 13). Among these cases, the nonlinear Kerr effect induced all-optical modulation in the Si-rich SiN_x with $R = 0.5$ is extremely weak due to its smallest nonlinear refractive index. The

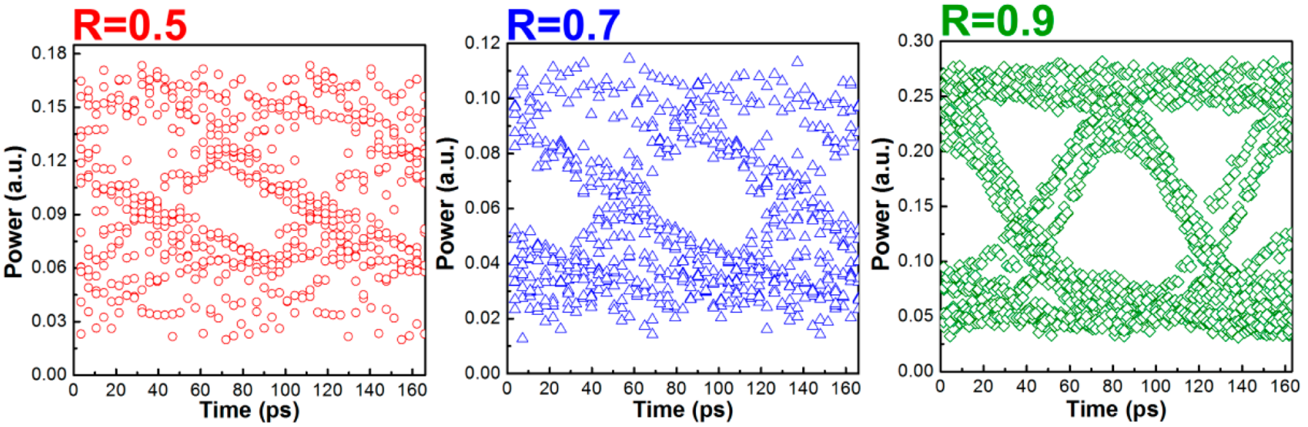

Figure 14. Repeatedly stacked trace of the inverted 12 Gbit/s pulsed RZ-OOK data stream obtained at the probe output from the Si-rich SiN_x microring resonator.

converted probe data amplitude is increased from 10 mV to 75 mV by reducing the Si/N composition from 1.53 to 2.06, corresponding to the enhancement of conversion efficiency from 13.3 mV/W to 100 mV/W when increasing the Si concentration from 59.1% to 66.2% in the Si-rich SiN_x microring resonator.

Figure 14 shows the 12 Gbit/s pulsed RZ-OOK eye diagrams of the data-format inverted probe data stream for all of the Si-rich SiN_x microring resonators based all-optical cross-wavelength data converters, which are obtained by artificially piling the inverted 12 Gbit/s pulsed RZ-OOK data stream captured from the digital sampling oscilloscope (Agilent 86100A +83485A). The format-inverted probe data stream in the Si-rich SiN_x microring resonator grown with the lowest SiH_4/NH_3 fluence ratio ($R = 0.5$) shows an almost blurred eye diagram, in which the signal-to-noise ratio (SNR) of the format-inverted data stream obtained from the Si-rich SiN_x microring resonator is too difficult to be measured. In contrast, the eye diagram of the format-inverted probe data stream becomes clear by using the Si-rich SiN_x microring resonators with $R = 0.7$ and $R = 0.9$, and the measured SNRs are increased to 4.7 and 7.5 dB, respectively. In more detail, the timing jitter of ~24 ps for the format-inverted probe data stream is not deviated much from that of the pump data stream. Such an enhancement on the SNR of the Si-rich SiN_x microring resonator converted data stream can be correlated with the greatly enhanced nonlinear refractive index of the Si-rich SiN_x (from 1.4×10^{-14} to 1.6×10^{-13} cm^2/W). When increasing the excess Si concentration in Si-rich SiN_x films by detuning R from 0.5 to 0.9, the transient wavelength shift induced by the nonlinear Kerr effect is also increased from 0.02 nm to 0.07 nm. Accordingly, the induced maximal transmittance change significantly enlarges from 9% to 72%, which makes the modulation depth and the amplitude of the cross-wavelength-modulated probe data stream from the Si-rich SiN_x microring resonator with $R = 0.9$ larger than other cases. Moreover, the rising/falling time of 29 ps obtained from the format-inverted probe data stream obtained from the Si-rich SiN_x with $R = 0.9$ is similar to that extracted from the pump data stream. It indicates that the Si-rich SiN_x microring resonator can perfectly cross-wavelength modulate the probe carrier to implement the format-preserved or -inverted data conversion without distortion. In reality, the maximal modulation bandwidth of the Si-rich SiN_x-based all-optical Kerr switching is mainly determined by the quality factor of the microring resonator; however, a trade-off between the modulation response and the quality factor is set due to their nonlinear dependency. The photon lifetime of the Si-rich SiN_x microring resonator is 19 ps, as given by $\tau_p \approx Q\lambda_0/2\pi c$ with $Q \approx 24019$ and $\lambda_0 = 1550$ nm, which decides the maximal modulation bandwidth of the Si-rich SiN_x-based all-optical Kerr switch as high as 50 GHz. Such a broadened bandwidth guarantees the high-speed all-optical data conversion and format inversion of the data stream in the Si-rich SiN_x microring resonator. The demonstration in this work has enabled the Si-rich SiN_x microring resonator as a new class of all-optical nonlinear Kerr switch that is capable of serving as the wavelength converter and data-format inverter for future all-optical interconnected communication integrated circuits.

Conclusion. By using the Si-rich SiN_x microring resonator with its optical nonlinear Kerr effect enhanced by tuning the Si/N ratio, the cross-wavelength all-optical data conversion and format inversion at 12 Gbit/s have been successfully demonstrated. The microring resonators are made by three PECVD-grown Si-rich SiN_x samples with $R = 0.5$, $R = 0.7$, and $R = 0.9$, providing the transmission spectra periodically turned off by notched dip responses with a quality factor of $>2.4 \times 10^4$. By scanning the probe wavelength around the notched spectral response of the Si-rich SiN_x microring resonator, the transient spectral shift induced by the ultrafast nonlinear Kerr effect under intense pumping is utilized to demonstrate the cross-wavelength all-optical data conversion with either the sign preserved or the inverted data format. The nonlinear Kerr switching induced wavelength shifts of the transmission dips are temporally red-shifted by 0.02 and 0.1 nm under intense laser pulse excitation for the Si-rich SiN_x microring resonators with $R = 0.5$ and $R = 0.9$. On the basis of the wavelength shift, the refractive index change induced by the nonlinear Kerr effect is estimated to increase from 2×10^{-5} to 1.6×10^{-4} for the Si-rich SiN_x with a fluence ratio increase from $R = 0.5$ to $R = 0.9$, indicating that the nonlinear refractive index at ~1550 nm is enhanced from 1.4×10^{-14} to 1.6×10^{-13} cm^2/W by increasing the excess Si concentration in the SiN_x film from 59.1% to 66.2%. As a result, the cross-wavelength all-optical pulsed RZ-OOK data conversion with sign preserved or inversed format can be achieved by enhancing the nonlinear Kerr effect in the Si-rich SiN_x microring resonator. With reducing the Si/N composition ratio from 1.53 to 2.06, the all-optical converted data amplitude on the modulated probe is significantly increased from 10 mV to 75 mV, similarly leading to the enhancement of the all-optical conversion efficiency from 13.3

mV/W to 100 mV/W in the Si-rich SiN$_x$ microring resonator. The converted probe data reveal a similar rising/falling time of 29 ps with the incoming pump data, indicating that the data can be cross-wavelength converted without distortion at a bit rate as high as 12 Gbit/s. The upper limitation on the modulation bandwidth of 50 GHz is estimated by the photon lifetime of 19 ps in the Si-rich SiN$_x$ microring resonator.

METHODS

Experimental Setup for the Data Conversion. The experimental setup of the nonlinear Kerr switch based all-optical data converter/inverter is described below. The pump pulse is generated by externally modulating a continuous-wave tunable laser (TL1, HP, 8168F) at 1550 nm with a Mach–Zehnder modulator (MZM, JDSU, 10024180, biased point offset at V_{dc} = 6.4 V). A user-defined electrical 12 Gbit/s pseudo random binary sequence RZ-OOK data stream with a pattern length of 2^7-1 is generated from an arbitrary waveform generator (Tektronix, AWG 7122) with a sampling rate of 12 Gbit/s and an analog bandwidth of 6 GHz. Concurrently, the electrical pump pulse is boost amplified by an RF amplifier (EA, JDSU, H301) to drive the MZM for pulsating the continuous-wave tunable laser output. The pulse width and repetition rate of the electrical pulse are set as 83 ps and 12 MHz, respectively. Subsequently, the generated optical pulse is power amplified by using a first-stage erbium-doped fiber amplifier (EDFA1, JDSU, OAB1552 + 20FA6), and an optical bandpass filter (OBPF1, SANTEC, OTF-910) with a 3 dB line width of 0.4 nm is utilized to suppress the induced amplified spontaneous emission noise during first-stage amplification. Another high-gain EDFA (EDFA2, SDO, EFAH1B111NC02) serves as the second-stage boost optical amplifier to further increase the peak power of the pump pulse, and an OBPF (OBPF2, JDS, TB1500B) with a 3 dB line width of 5 nm is also utilized to suppress the ASE noise induced by the second-stage EDFA. Finally, the dual-stage amplified pump pulse with a pulse width of 83 ps and a peak power of up to 3 W is delivered for the test.

To perform the cross-wavelength data conversion and format inversion, a continuous-wave probe signal generated from a tunable laser (TL2, Agilent, 8164A) is amplified by an EDFA (EDFA3, SDO, SEL). Two polarization controllers are used to adjust the polarization of the pump and probe signals individually. By coupling the pump and probe signals into the Si-rich SiN$_x$ microring resonator through a lensed fiber with a mode-field diameter of 2 μm and adjusting the wavelength of the pump data stream to coincide with the resonance peak of the microring resonator, the maximal intensity magnification of the coupled pump beam is achieved to induce the largest nonlinear Kerr effect. Afterward, the cross-wavelength-modulated probe signal is coupled out and collected by a lensed fiber at the output facet of the Si-rich SiN$_x$ bus waveguide. In order to distinguish the probe from the pump at the receiving port, an OBPF (OBPF3, JDS, TB1500B) was used to filter out the pump data stream and the cross-wavelength-modulated probe data stream. The separated probe data stream is sent into a photodetector (Notel, pp-10G). Consequently, the traces and eye diagrams of the cross-wavelength-modulated probe data stream are resolved by a digital sampling oscilloscope (Agilent, 86100A+83485A).

Design Principle. The all-pass microring resonator is constructed by a directional bus coupler and a microring cavity. Assuming that the insertion loss is negligible in the directional coupler and the bus/ring waveguides exhibit identical geometries at input and output ports, the transfer matrix function between the input (A_{in}, B_{in}) and output (A_{out}, B_{out}) optical fields is described by[42]

$$\begin{bmatrix} A_{out} \\ B_{out} \end{bmatrix} = \begin{bmatrix} \cos(\kappa l) & -j\sin(\kappa l) \\ -j\sin(\kappa l) & \cos(\kappa l) \end{bmatrix} \begin{bmatrix} A_{in} \\ B_{in} \end{bmatrix} \tag{2}$$

where κ is the coupling coefficient of the directional coupler and l is the coupling length between the directional coupler and the microring resonator. The output optical field from the microring waveguide is given by

$$B_{out} = B_{in} \exp\left(\frac{\alpha_{ring}}{2} + j\beta L\right) \tag{3}$$

where α_{ring} is the loss coefficient of the microring resonator, $\beta = 2\pi n_g L/\lambda$ is the propagation constant, n_g is the group index of the waveguide, λ is the central wavelength, and L is the cavity length. By correlating eqs 2 and 3, the transmittance of the all-pass microring resonator is given by

$$T(\lambda) = \left|\frac{A_{out}}{A_{in}}\right|^2 = 1 - \frac{(1 - e^{-\alpha_{ring}L})[1 - \cos^2(\kappa l)]}{[1 - e^{-\alpha_{ring}L/2}\cos(\kappa l)]^2 + 4e^{-\alpha_{ring}L/2}\cos(\kappa l)\sin^2\left(\frac{\pi n_g L}{\lambda}\right)} \tag{4}$$

With the 3 dB line width (δf) of the microring resonator determined by solving eq 4, the corresponding analytic solution for the quality factor (Q) of the microring resonator is derived as

$$Q = \frac{\Delta f}{\delta f} = \frac{c}{n_g L}\left[\frac{c(1 - e^{-\alpha_{ring}L/2}\cos(\kappa l))}{\pi n_g L\sqrt{e^{-\alpha_{ring}L/2}\cos(\kappa l)}}\right]^{-1} \tag{5}$$

Particularly, the optical intensity can be enhanced when the propagation wavelength is exactly located at the resonant wavelength of the microring resonator. The traveling wave in the microring waveguide interferes constructively with the input optical field, and the optical intensity magnification is built up in the microring resonator when the optical field travels with a phase-shift of an integral multiple of 2π in one round trip. By defining K as the coupling ratio between the bus and microring waveguides, the intensity magnification factor (M) of the microring resonator is defined as

$$\begin{aligned} M &= \left|\frac{B_{in}}{A_{in}}\right|^2 \\ &= \left|\frac{-j\sin(\kappa l)\exp\left(-\frac{\alpha_{ring}}{2}L\right)}{1 - \cos(\kappa l)\exp\left(-\frac{\alpha_{ring}}{2}L\right)}\right|^2 \\ &= \left|\frac{-\mathrm{K}\exp\left(-\frac{\alpha_{ring}}{2}L\right)}{1 - \sqrt{1 - \mathrm{K}^2}\exp\left(-\frac{\alpha_{ring}}{2}L\right)}\right|^2 \end{aligned} \tag{6}$$

DOI: 10.1021/acsphotonics.5b00192
ACS Photonics 2015, 2, 1141–1154

AUTHOR INFORMATION

Corresponding Author

*Phone: +886-2-33663700, ext 6519. Fax: +886-2-33669598. E-mail: grlin@ntu.edu.tw.

Notes

The authors declare no competing financial interest.

ACKNOWLEDGMENTS

This work was supported by the Ministry of Science and Technology, Taiwan, R.O.C., under grants NSC 101-2221-E-002-071-MY3, MOST 103-2221-E-002-042-MY3, and MOST 104-2221-E-002-117-MY3.

REFERENCES

(1) Soref, R. A.; Bennett, B. R. Electrooptical effects in silicon. *IEEE J. Quantum Electron.* **1987**, *QE-23*, 123−129.

(2) Reed, G. T.; Mashanovich, G. F.; Gardes, Y.; Thomson, D. J. Silicon optical modulators. *Nat. Photonics* **2010**, *4*, 518−526.

(3) Almeida, V. R.; Barrios, C. A.; Panepucci, R. R.; Lipson, M.; Foster, M. A.; Ouzounov, D. G.; Gaeta, A. L. All-optical switching on a silicon chip. *Opt. Lett.* **2004**, *29*, 2867−2869.

(4) Li, C.; Luo, X.; Poon, A. W. Dual-microring-resonator electro-optic logic switches on a silicon chip. *Semicond. Sci. Technol.* **2008**, *23*, 064010.

(5) Först, M.; Niehusmann, J.; Plötzing, T.; Bolten, J.; Wahlbrink, T.; Moormann, C.; Kurz, H. High-speed all-optical switching in ion-implanted silicon-on-insulator microring resonators. *Opt. Lett.* **2007**, *32*, 2046−2048.

(6) Schmidt, B.; Xu, Q.; Shakya, J.; Manipatruni, S.; Lipson, M. Compact electro-optic modulator on silicon-on-insulator substrates using cavities with ultra-small modal volumes. *Opt. Express* **2007**, *15*, 3140−3148.

(7) Chen, L.; Preston, K.; Manipatruni, S.; Lipson, M. Integrated GHz silicon photonic interconnect with micrometer-scale modulators and detectors. *Opt. Express* **2009**, *17*, 15248−15256.

(8) Linnros, J. Carrier lifetime measurements using free carrier absorption transients. II. Lifetime mapping and effects of surface recombination. *J. Appl. Phys.* **1998**, *84*, 284−291.

(9) Claps, R.; Raghunathan, V.; Dimitropoulos, D.; Jalali, B. Influence of nonlinear absorption on Raman amplification in Silicon waveguides. *Opt. Express* **2004**, *12*, 2774−2780.

(10) Kekatpure, R.; Brongersma, M. Quantification of free-carrier absorption in silicon nanocrystals with an optical microcavity. *Nano Lett.* **2008**, *8*, 3787−3793.

(11) Kekatpure, R.; Brongersma, M. Near-infrared free-carrier absorption in silicon nanocrystals. *Opt. Lett.* **2009**, *34*, 3397−3399.

(12) Marchena, E.; Redding, B.; Creazzo, T.; Prather, D. Mitigation of Si nanocrystal free carrier absorption loss at 1.5 μm in a concentric microdisk structure. *Opt. Lett.* **2010**, *35*, 2182−2184.

(13) Wu, C.-L.; Lin, G.-R. Inhomogeneous linewidth broadening and radiative lifetime dispersion of size dependent direct bandgap radiation in Si quantum dot. *AIP Adv.* **2012**, *2*, 042162.

(14) Cheng, C.-H.; Lien, Y.-C.; Wu, C.-L.; Lin, G.-R. Mutlicolor electroluminescent Si quantum dots embedded in SiO_x thin film MOSLED with 2.4% external quantum efficiency. *Opt. Express* **2013**, *21*, 391−403.

(15) Creazzo, T.; Redding, B.; Marchena, E.; Shi, S.; Prather, D. Free-carrier absorption modulation in silicon nanocrystal slot waveguides. *Opt. Lett.* **2010**, *35*, 3691−3693.

(16) Wu, C.-L.; Su, S.-P.; Lin, G. R. All-optical data inverter based on free-carrier absorption induced cross-gain modulation in Si quantum dot doped SiO_x waveguide. *IEEE J. Sel. Top. Quantum Electron.* **2014**, *20*, 8200909.

(17) Wu, C.-L.; Su, S.-P.; Lin, G. R. All-optical modulation based on silicon quantum dot doped SiO_x:Si-QD waveguide. *Laser Photonics Rev.* **2014**, *8*, 766−776.

(18) Prakash, G. V.; Cazzanelli, M.; Gaburro, Z.; Pavesi, L.; Iacona, F.; Franzo, G.; Priolo, F. Nonlinear optical properties of silicon nanocrystals grown by plasma-enhanced chemical vapor deposition. *J. Appl. Phys.* **2002**, *91*, 4607−4610.

(19) Hernández, S.; Pellegrino, P.; Martínez, A.; Lebour, Y.; Garrido, B.; Spano, R.; Cazzanelli, M.; Daldosso, N.; Pavesi, L.; Jordana, E.; Fedeli, J. M. Linear and nonlinear optical properties of Si nanocrystals in SiO_2 deposited by plasma-enhanced chemical-vapor deposition. *J. Appl. Phys.* **2008**, *103*, 064309.

(20) Spano, R.; Daldosso, N.; Cazzanelli, M.; Ferraioli, L.; Tartara, L.; Yu, J.; Degiorgio, V.; Jordana, E.; Fedeli, J. M.; Pavesi, L. Bound electronic and free carrier nonlinearities in silicon nanocrystals at 1550 nm. *Opt. Express* **2009**, *17*, 3941−3950.

(21) Ito, M.; Imakita, K.; Fujii, M.; Hayashi, S. Nonlinear optical properties of silicon nanoclusters/nanocrystals doped SiO_2 films: Annealing temperature dependence. *J. Appl. Phys.* **2010**, *108*, 063512.

(22) Lin, G.-R.; Su, S.-P.; Wu, C.-L.; Lin, Y. H.; Huang, B.-J.; Wang, H.-Y.; Tsai, C.-T.; Wu, C.-I; Chi, Y.-C. Si-rich SiN_x based Kerr switch enables optical data conversion up to 12 Gbit/s. *Sci. Rep.* **2015**, *5*, 9611.

(23) Chen, R.; Lin, D. L.; Mendoza, B. Enhancement of the third-order nonlinear optical susceptibility in Si quantum wires. *Phys. Rev. B: Condens. Matter Mater. Phys.* **1993**, *48*, 11879−11882.

(24) Blasco, J.; Galán, J. V.; Sanchis, P.; Martínez, J. M.; Martínez, A.; Jordana, E.; Fedeli, J. M.; Martí, J. FWM in silicon nanocrystal-based sandwiched slot waveguides. *Opt. Commun.* **2010**, *283*, 435−437.

(25) Trita, A.; Lacava, C.; Minzioni, P.; Colonna, J.-P.; Gautier, P.; Fedeli, J.-M.; Cristiani, I. Ultra-high four wave mixing efficiency in slot waveguides with silicon nanocrystals. *Appl. Phys. Lett.* **2011**, *99*, 191105.

(26) Martinez, A.; Blasco, J.; Sanchis, P.; Galan, J. V.; Garcia-Ruperez, J.; Jordana, E.; Gautier, P.; Lebour, Y.; Hernandez, S.; Spano, R.; Guider, R.; Daldosso, N.; Garrido, B.; Fedeli, J. M.; Pavesi, L.; Marti, J. Ultrafast all-optical switching in a silicon-nanocrystal-based silicon slot waveguide at telecom wavelengths. *Nano Lett.* **2010**, *10*, 1506−1511.

(27) Ikeda, K.; Saperstein, R.-E.; Alic, N.; Fainman, Y.; Thermal. and Kerr nonlinear properties of plasma-deposited silicon nitride/ silicon dioxide waveguides. *Opt. Express* **2008**, *16*, 12987−12994.

(28) Levy, J.-S.; Gondarenko, A.; Foster, M.-A.; Turner-Foster, A.-C.; Gaeta, A.-L.; Lipson, M. CMOS-compatible multiple-wavelength oscillator for on-chip optical interconnects. *Nat. Photonics* **2010**, *4*, 37−40.

(29) Tan, D. T. H.; Ikeda, K.; Sun, P. C.; Fainman, Y. Group velocity dispersion and self phase modulation in silicon nitride waveguides. *Appl. Phys. Lett.* **2010**, *96*, 061101.

(30) Lin, G.-R.; Lin, Y. H.; Pai, Y.-H.; Meng, F.-S. Si nanorod length dependent surface Raman scattering linewidth broadening and peak shift. *Opt. Express* **2011**, *19*, 597−605.

(31) Viera, G.; Huet, S.; Boufendi, L. Crystal size and temperature measurements in nanostructured silicon using Raman spectroscopy. *J. Appl. Phys.* **2001**, *90*, 4175−4183.

(32) Sheng, S.; Liao, X.; Kong, G.; Han, H. Study of microstructure of high stability hydrogenated amorphous silicon films by Raman scattering and infrared absorption spectroscopy. *Appl. Phys. Lett.* **1998**, *73*, 336−338.

(33) Dinu, M.; Quochi, F.; Garcia, H. Third-order nonlinearities in silicon at telecom wavelengths. *Appl. Phys. Lett.* **2003**, *82*, 2954−2956.

(34) Cho, H. J.; Lin, A.; Moon, S.; Han, W. T. Non-resonant optical nonlinearity of germane-silicate optical fiber incorporated with Si nanocrystals. *J. Korean Phys. Soc.* **2008**, *53*, 1565−1569.

(35) Nie, W. Optical nonlinearity: phenomena, applications, and materials. *Adv. Mater.* **1993**, *5*, 520−545.

(36) Spence, D. E.; Kean, P. N.; Sibbett, W. 60-fsec pulse generation from a self-mode-locked Ti:sapphire laser. *Opt. Lett.* **1991**, *16*, 42−44.

(37) Chen, R.; Lin, D. L.; Mendoza, B. Enhancement of the third-order nonlinear optical susceptibility in Si quantum wires. *Phys. Rev. B: Condens. Matter Mater. Phys.* **1993**, *48*, 11879−11882.

(38) Justus, B. L.; Ruller, J. A. Nonresonant optical nonlinearity of quantum-confined nanocrystals of CuBr in glass. *Opt. Mater.* **1993**, *2*, 33−37.

(39) Kurian, P. A.; Vijayan, C.; Sathiyamoorthy, K.; Sandeep, C. S.; Philip, R. Excitonic transitions and off-resonant optical limiting in CdS quantum dots stabilized in a synthetic glue matrix. *Nanoscale Res. Lett.* **2007**, *2*, 561−568.

(40) Wang, Y.; Yang, X.; He, T. C.; Gao, Y.; Demir, H. V.; Sun, X. W.; Sun, H. D. Near resonant and nonresonant third-order optical nonlinearities of colloidal InP/ZnS quantum dots. *Appl. Phys. Lett.* **2013**, *102*, 021917.

(41) López-Suárez, A.; Torres-Torres, C.; Rangel-Rojo, R.; Reyes-Esqueda, J. A.; Santana, G.; Alonso, J. C.; Ortiz, A.; Oliver, A. Modification of the nonlinear optical absorption and optical Kerr response exhibited by nc-Si embedded in a silicon-nitride film. *Opt. Express* **2009**, *17*, 10056−10068.

(42) Bogaerts, W.; De Heyn, P.; Van Vaerenbergh, T.; De Vos, K.; Selvaraja, S. K.; Claes, T.; Dumon, P.; Bienstman, P.; Van Thourhout, D.; Baets, R. Silicon microring resonators. *Laser Photonics Rev.* **2012**, *6*, 47−73.